Comparison between MAP and Post-processed ML for Incorporating Anatomical Knowledge in Emission Tomography.

Johan Nuyts, Kristof Baete,Dirk Bequé,and Patrick Dupont

Abstract— **Previously, the noise characteristics obtained with penalized likelihood reconstruction (or maximum-a-posteriori, MAP) have been compared to those obtained with post-smoothed maximum-likelihood (ML) reconstruction, for applications requiring uniform resolution. It was found that penalized-likelihood reconstruction was not superior to post-smoothed ML. In this study a similar comparison is made, but now for applications where the noise suppression is tuned with anatomical information. Our simulations reveal that "straightforward" post-processing of the ML reconstruction results in inferior performance. It is hypothesized that this is due to the noise correlations between neighboring pixels, and an approximate prewhitening filter is derived. The efficacy of the prewhitening filter is illustrated with simulations. When this prewhitening filter was incorporated in the post-processing method, the performance became similar to that of MAP.**

I. INTRODUCTION

IN previous studies, the noise performance of post-smoothed maximum-likelihood (ML) reconstruction has been compared to that of penalized-likelihood (PL) reconstruction, for emission tomography applications requiring "uniform" spatial resolution [1], [2]. Here, resolution is considered uniform if the local impulse response has spherical symmetry and is independent of the object and of the position in the image. The results indicated that noise suppression with PL is not superior to that with post-smoothed ML for these applications; a theoretical argument is given in [2].

There is an increasing interest in the combination of anatomical and functional information. Promising results have been obtained with maximum-a-posteriori (MAP) reconstruction, by using the anatomical information to modify the prior as a function of position. In such images, the resolution is strongly position and orientation dependent, and therefor, the conclusions of the studies mentioned above may not apply. In this work, we study the noise characteristics obtained with MAP reconstruction using anatomical priors, with those obtained with post-processing the unconstrained ML reconstruction.

The following section describes the MAP and post-processing methods, designed to improve the reconstruction by using anatomical information. Then, an approximate prewhitening filter is derived, and it is shown how the post-processing method can be improved to deal with noise correlations, by incorporation of this filter. In the third section, two simulation experiments are described. The first experiment validates the prewhitening filter, by showing that the numerical non-prewhitening observer performs better when the images have been filtered. The second experiment compares MAP reconstruction with the two post-processing methods (the "straightforward" method and the method with prewhitening). The methods are compared by applying a numerical observer to detect cold lesions. The findings are discussed in section four.

II. THEORY

To study MAP reconstruction with an anatomy-based prior, we consider a phantom consisting of 3 different tissue classes and one background class. The classes are known from an anatomical image, the activity has to be reconstructed from noisy sinogram data. This phantom is inspired by ongoing work on brain imaging with PET in epilepsy [3], where the three classes are gray matter, white matter and cerebrospinal fluid (CSF). The three classes will be denoted accordingly as G for gray matter, W for white matter and C for CSF. Lesions of reduced tracer uptake are only expected in G. The expected tracer uptake for C is zero, the tracer uptake in W is expected to be uniform, but with unknown mean. Extension to objects with different number of classes and different class features is straightforward.

A. Reconstruction

An unconstrained maximum-likelihood reconstruction can be obtained by searching the activity $\Lambda = \{\lambda_j\}$ that maximizes the logarithm of the likelihood, $L(Y, \Lambda)$:

$$L(Y, \Lambda) = \sum_i y_i \ln(\sum_j a_{ij}\lambda_j + t_i) - (\sum_j a_{ij}\lambda_j + t_i), \quad (1)$$

where y_i is the count level in detector i, λ_j is the activity in pixel j, a_{ij} is the probability that activity in j contributes to the count level in detector i, t_i is the expected contribution due to e.g. randoms or scatter, and terms independent of λ_j have been omitted. As argued in [1], [2], a post-smoothed version of the maximum-likelihood image has excellent resolution and noise characteristics, which can be obtained by applying a high number of iterations of the EM [4] or OS-EM algorithm [5].

Work supported by K.U.Leuven grants OT-00/32 and IDO-99/005, and F.W.O. grant G.0174.03

Nuclear Medicine, K.U.Leuven, B-3000 Leuven, Belgium. (e-mail: Johan.Nuyts@uz.kuleuven.ac.be)

It is assumed that available anatomical knowledge can be represented with a single label in every pixel j, partial volume effects [3] will not be considered here. The anatomical information is exploited by combining the likelihood with a prior. The logarithm of the prior equals $M_G + M_W + M_C$:

$$\begin{aligned} M_G(\Lambda) &= \sum_{j\in G}\sum_{k\in G} -\beta_G \alpha_{j-k} \frac{(\lambda_j-\lambda_k)^2}{\lambda_j+\lambda_k+\gamma|\lambda_j-\lambda_k|} && (2)\\ M_W(\Lambda) &= -\beta_W \sum_{j\in W}(\lambda_j - \mathrm{mean}_W(\Lambda))^2 && (3)\\ M_C(\Lambda) &= -\beta_C \sum_{j\in C}(\lambda_j)^2, && (4)\end{aligned}$$

where G, W and C are the classes, and β_G, β_W and β_C are parameters determining the prior strength for each class. The weight α_{j-k} defines the neighborhood; we used $\alpha_{j-k} = 1$ for horizontal and vertical neighbors j and k, and $\alpha_{j-k} = 0$ otherwise. The function mean_W returns the mean value over the class W. M_G is a prior favoring smoothness by penalizing relative differences between pixels [6]. M_W favors smoothness by penalizing the deviations from the mean of class W, and M_C penalizes differences from zero. The reconstruction Λ is obtained by maximizing $L(Y,\Lambda)+M_G(\Lambda)+M_W(\Lambda)+M_C(\Lambda)$. In the experiments described below, this is done with the gradient ascent algorithm described in [6].

B. Post-processing the ML-image

The simplest way to incorporate the anatomical information into the unconstrained ML-reconstruction would be to smooth the image with a low pass filter, restricting the support of the filter to a single class. However, it would be difficult to obtain a similar smoothing effect as that of the prior in the MAP approach, and performance comparisons would not be obvious. To avoid these problems, the smoothing in the post-processing approach has been implemented with the same prior as in the MAP method. For that purpose, an artificial likelihood term $Q_1(X,\Lambda)$ is introduced, which penalizes deviations between the unconstrained ML-reconstruction X and the processed image Λ:

$$Q_1(\Lambda) = -\beta_Q \sum_j (x_j - \lambda_j)^2, \tag{5}$$

where $x_j \in X$ represents the unconstrained ML-image, $\lambda_j \in \Lambda$ is the final, post-processed image and β_Q is a parameter defining the strength of the “likelihood”. The post-processed image Λ is found by maximizing the objective function $Q_1 + M_G + M_W + M_C$. To obtain a similar smoothing effect as with MAP-reconstruction, the relative strength of the prior should be the same in both methods. It is not clear how β_Q can be chosen to ensure this. Instead, the relative strength of the prior is varied for both methods in the experiments, and the maxima of the resulting performance curves are compared.

The objective function Q_1 can be improved by taking into account the noise correlations in the ML-image. A similar problem arises in the implementation of numerical observers, described in the next section.

C. Numerical observers

Assume that the observer exactly knows the noiseless images $\bar\Lambda_1$ and $\bar\Lambda_0$, which are the images with and without the signal respectively. The task is to decide if the signal is present in a noisy image Λ. Assume also that the noise covariance matrix C_Λ is known and independent of the signal. In this situation, the ideal (prewhitening) observer computes the statistic

$$\begin{aligned} q_{\mathrm{pw}} &= (\bar\Lambda_1 - \bar\Lambda_0)' C_\Lambda^{-1} \Lambda. && (6)\\ &= (C_\Lambda^{-1/2}\bar\Lambda_1 - C_\Lambda^{-1/2}\bar\Lambda_0)' C_\Lambda^{-1/2}\Lambda. && (7)\end{aligned}$$

The signal-to-noise ratio (SNR) of q_{pw} can be computed from Monte Carlo simulations, and is a measure of the performance of the ideal observer [7]. Equation (7) states that the ideal observer first applies the prewhitening (PW) filter $C_\Lambda^{-1/2}$, and then applies a matched filter to detect the signal [7].

In the experiments described below, the nonprewhitening observer has been used to evaluate lesion detection performance. It is identical to the ideal observer, under the assumption that the noise is uniform and uncorrelated:

$$q_{\mathrm{npw}} = (\bar\Lambda_1 - \bar\Lambda_0)'\Lambda. \tag{8}$$

D. Approximate prewhitening

Because MLEM is not an efficient estimator, the inverse of the covariance matrix does not equal the Fisher information matrix [8], [9], [10]. Several authors have simply used the Fisher information matrix as an approximation for the inverse covariance matrix, with good results [1], [11], [12], [13].

With this approximation, (7) becomes:

$$q_{\mathrm{pw}} \simeq (F^{1/2}\bar\Lambda_1 - F^{1/2}\Lambda_0)' F^{1/2}\Lambda, \tag{9}$$

where F is the Fisher information matrix. F is positive semi-definite, so $F^{1/2}$ exists. We propose two different additional approximations to obtain a filter that is tractable in practice.

1) Local optimisation (filter F_1): If the position of the lesion is approximately known a-priori, we can attempt to achieve good local performance by computing a shift invariant filter F_1, that is (nearly) identical to F at that particular position in the image. This is obtained by replacing all rows (or columns) of the matrix F with shifted versions of the row (or column) j, where j is the pixel index corresponding to the lesion position. Then, $F_1^{1/2}$ can be computed using the Fourier transform, since F_1 is shift invariant [12].

The elements of the Fisher information matrix for ML-reconstruction equal [8], [9]:

$$F(j,k) = \sum_i \frac{a_{ij}a_{ik}}{\bar y_i}, \tag{10}$$

where $\bar y_i$ is the expectation of y_i. For a fixed point $j = \gamma$, $F(j,k)$ is an image with the same size as the reconstruction image. The filter F_1 is then obtained as

$$F_1 = \mathrm{FT}^{-1}\sqrt{\mathrm{FT}(F_{j=\gamma,.})}, \tag{11}$$

where the squareroot is applied on a pixel basis and FT denotes 2D Fourier transform. F_1 is a low-pass filter kernel, with an

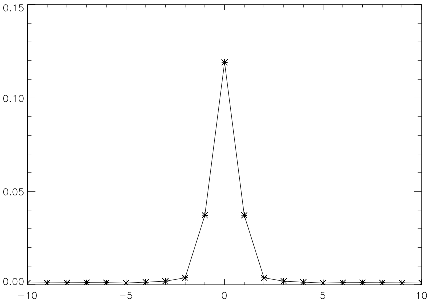

Fig. 1. Radial profile of the 2D convolution kernel of the shift invariant and data independent prewhitening kernel F_2. The FWHM is 1.5 pixels.

approximate shape of $1/|f|^{1/2}$ in the frequency domain, but the exact shape depends on the tracer distribution, the attenuation and the detector resolution. In practice, it suffices to extract a small convolution mask centered about the maximum.

2) Shift invariant and data independent approximation (filter F_2): In clinical practice, the position of the lesion is usually unknown. In addition, for some applications it may be preferable to have a predictable, object-independent and circularly symmetrical point spread function. For that purpose, we calculate the shape of the filter in absence of attenuation and in the center of a uniform object. In that case $\bar{y}_i$ becomes an irrelevant constant in (10). The computation is the same as above, but without the division by $\bar{y}_i$, and without position dependencies (attenuation, position dependent blurring) in the system matrix $[a_{ij}]$. A profile through the resulting filter kernel F_2 in the spatial domain is shown in figure 1 for a projector with ideal resolution: it is sharp in the center, but decays only slowly to zero. The full width at half maximum (FWHM) is about 1.5 pixels.

E. Post-processing with prewhitening

The “likelihood” of expression (5) ignores the correlations between neighboring pixels. A more accurate measure for similarity with the ML-reconstruction is:

$$Q(\Lambda) = -\beta_Q (X - \Lambda)' C_X^{-1} (X - \Lambda). \qquad (12)$$

Approximating the inverse of the covariance with the Fisher information matrix yields

$$\begin{aligned} Q_2(\Lambda) &= -\beta_Q (X - \Lambda)' F (X - \Lambda) \\ &= -\beta_Q (F^{1/2}(X - \Lambda))' F^{1/2} (X - \Lambda). \qquad (13) \end{aligned}$$

It is interesting to see the relation between Q_2 and the likelihood $L(Y, \Lambda)$. With A the system matrix and C_Y the covariance matrix of the sinogram data Y, we have:

$$\begin{aligned} Q_2(\Lambda) &= -\beta_Q (X - \Lambda)' A' C_Y^{-1} A (X - \Lambda) \\ &= -\beta_Q (AX - A\Lambda)' C_Y^{-1} (AX - A\Lambda), \qquad (14) \end{aligned}$$

which is the Gaussian approximation of the Poisson likelihood $L(Y, \Lambda)$, if we can assume that $Y \simeq AX$. Note that this interpretation does not require that $F \simeq C_X^{-1}$.

The final image Λ is obtained by applying a gradient ascent algorithm to maximize $Q_2 + M_g + M_W + M_C$.

III. EXPERIMENTS

A. Experiment 1: approximate prewhitening

In this experiment, the efficacy of the approximate prewhitening filter is evaluated for unconstrained MLEM with postsmoothing. The approximate prewhitening filters described above are compared to Gaussian smoothing in a lesion detection experiment. Detection was done with the nonprewhitening numerical observer of eq (8).

In a first simulation, the Shepp-Logan phantom shown in figure 2 was used. The image contains 100 × 100 pixels, the three different activities were set to 4, 2 and 1 (figure 2). In the signal-present image, the activities in a small square region (16 pixels) were reduced with 20% (from 4 to 3.2). A noiseless sinogram was computed using 144 angles over 180 degrees, without attenuation and without blurring. Five thousand different Poisson noise realizations were computed, and each of those was reconstructed with the MLEM algorithm, accelerated with ordered subsets. A decreasing number of subsets was used to avoid convergence to a limit cycle: the scheme was (main iterations × number of subsets): $2 \times 36, 2 \times 24, 1 \times 16, 1 \times 12, 1 \times 8, 1 \times 4, 1 \times 1$, which is roughly equivalent to 161 regular MLEM iterations. Each reconstruction was post-smoothed with different filters, including a series of two dimensional Gaussian kernels, the filter F_1 (based on the Fisher information image for the center of the region), and the filter F_2, both of them with a mask size of 21×21. To evaluate the importance of the wide “tails” of the filter, we have also reduced the mask size for F_2 to 11×11 and 7×7.

In a second simulation, the same object was used, but a different region was studied (figure 2), and photon attenuation and finite resolution were included in the simulation and reconstruction. We used the attenuation of water at 511 keV (0.095 cm^{-1}), assuming a pixel size of 2.5 mm. Detector resolution was simulated by smoothing the projections with a Gaussian of 3 pixels FWHM. A larger (78 pixels), rectangular region was placed at the bottom of the phantom. Because of the excentric position, the filter F_1 is expected to be asymmetrical for this region, making it very different from the symmetrical F_2 kernel. Two thousand Poisson realizations were generated, reconstructed and analysed in the same way as for the first experiment. In the computation of the F_1 and F_2 kernels, the blurring was modeled in the detetion probabilities. As a result, the filters are wider than the one shown in figure 1.

B. Experiment 2: MAP and post-processed ML

This experiment compared MAP with post-processed ML. The same object as before was used. The relative activity in the three classes equals 3, 1 and 0. The effect of the algorithm on lesion detection was studied, where the lesion was a 20% decrease of activity in one of the four regions shown in fig 3. Five sinograms were computed: one with normal activity,

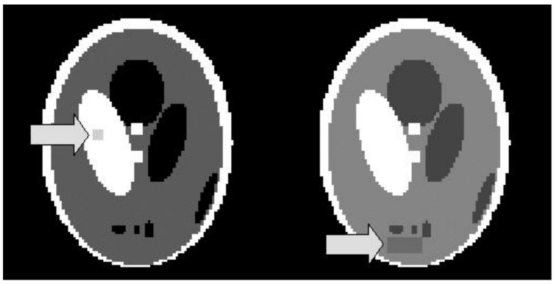

Fig. 2. The simulation objects with the signal (rectangular "lesion" of decreased perfusion) present. Left: simulation 1, right simulation 2.

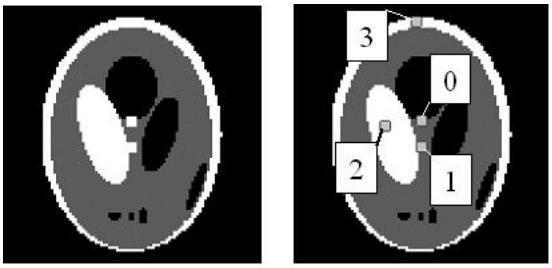

Fig. 3. Shepp-Logan phantom, consisting of 3 different anatomical components. In one of these, four regions are used to measure the signal-to-noise ratio for the detection of a 20% decrease in tracer uptake.

and four ones with a lesion (100 detectors × 144 angles, no attenuation, ideal point spread function). For each of those, 100 noise realizations were computed. For each noise realization, the output of the ideal observer was calculated, and images were reconstructed with the following algorithms: *1)* unconstrained MLEM post-smoothed with a Gaussian kernel; *2)* MAP; *3)* post-processed MLEM using the "likelihood" Q_1 of eq (5); *4)* post-processed MLEM using the "likelihood" Q_2 of eq (13), where $F^{1/2}$ was estimated using the approximate filter F_1. For ML, the width of the Gaussian kernel was varied. For the algorithms using the prior, the weight of the prior was varied. A wide range of the parameters was chosen such that an estimate of the maximum SNR for each algorithm could be obtained. For each region, and for each reconstruction algorithm (and for each of its parameters), the statistic for the nonprewhitening observer was computed using the reconstructions of the noise-free sinograms with and without signal to estimate $\bar{\Lambda}_1$ and $\bar{\Lambda}_0$ in (8). The SNR was computed from the mean and variance of the observer output for the 100 noise realizations.

IV. RESULTS

A. Experiment 1: approximate prewhitening

Figure 4 shows surface plots of the filter convolution kernels F_1 and F_2 for simulation 2. As expected, F_1 is markedly asymmetrical for this experiment. The FWHM of F_1 was 4.4 pixels horizontally, and 2.9 pixels vertically. In this experiment, a finite resolution of 3 pixels FWHM was used during simulation and reconstruction. The MLEM algorithm has attempted to correct for the blurring, causing stronger correlations between neighboring pixel values than in the first simulation. These correpond to a higher noise amplification for high spatial frequencies. As a result, the prewhitening filter has to smooth more, and the convolution kernel is wider (see figure 1).

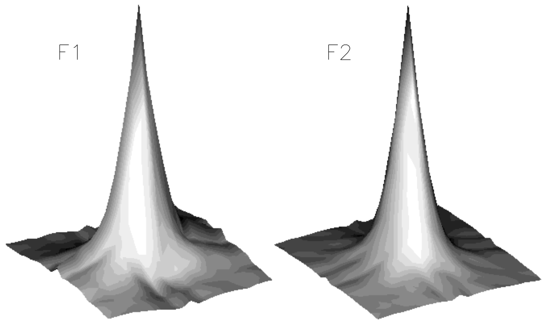

Fig. 4. The masks F_1 (left) and F_2 (right) for the second experiment.

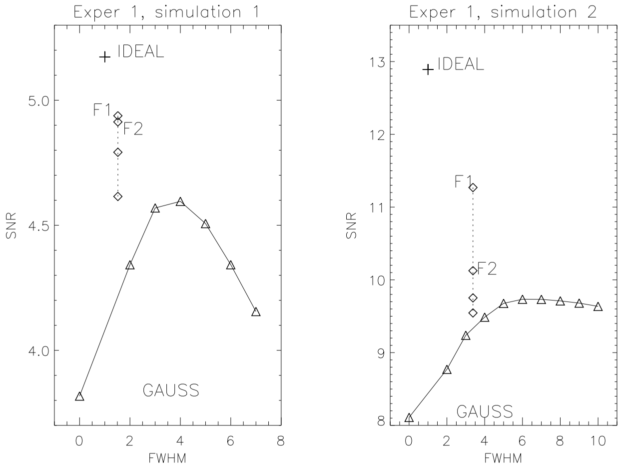

Fig. 5. The signal-to-noise ratios obtained for both simulations as a function of the FWHM of the filters. The SNR of the ideal observer is indicated as well. The solid line is for Gaussian postsmoothing. The dashed curve shows the SNR obtained with the F_1 mask, F_2 mask, and the F_2 masks with reduced size (11×11 and 7×7).

Figure 5 plots the SNR for the ideal observer and for the combination of MLEM with different post-smoothing filters, as a function of the FWHM of the filters. As expected, the SNR of the ideal observer is superior to that of post-smoothed MLEM. If Gaussian smoothing is applied, the nonprewhitening observer performs best with moderate smoothing. For both experiments, the nonprewhitening observer performs better after post-smoothing with F_1 than with any of the Gaussian filters. Approximating F_1 with the position independent kernel F_2 reduces the SNR, but for these experiments, it was still superior to that of any Gaussian filter. As mentioned before, F_1 was more asymmetrical in simulation 2 (fig. 4) than in simulation 1. As a result, F_2 was a poorer approximation of F_1 in simulation 2, and yielded a stronger loss of detection performance. Finally, decreasing the mask size of F_2 further reduced the SNR.

TABLE I

The maximum SNR for the four regions for post-smoothed ML, for MAP and for ML with post-processing based on the prior.

ROI	ideal	ML	MAP	ML and Q_1	ML and Q_2
0	6.4	6.0	6.0	4.9	5.8
1	5.9	5.3	5.4	4.1	5.3
2	6.0	5.1	5.1	4.8	5.2
3	7.5	6.7	6.8	5.6	6.5

B. *Experiment 2: MAP and post-processed ML*

The estimate for the maximum SNR for each of the algorithms is tabulated in table I. With 100 noise realizations, the error on the standard deviation is about 15%. The ideal observer is obviously superior. The post-processing method using Q_1 is outperformed by the three other algorithms.

V. Discussion

A straightforward way to incorporate anatomical information into the unconstrained MLEM image is to smooth the image, restricting the low pass filter to within object boundaries. This was implemented by combining the prior of eq. (2)-(4) with the similarity measure of (5). This approach ignores the correlations between neighboring pixels. Apparently, discarding information present in neighboring pixels at the other side of anatomical boundaries leads to a decreased signal to noise ratio (table I). Post-smoothed MLEM avoids the problem by smoothing over organ boundaries, but then the anatomical information remains unused. The MAP-algorithm avoids the problem by evaluating the current reconstruction in the sinogram space, where the noise is uncorrelated. Table I reveals no difference in signal-to-noise ratio between postsmoothed MLEM and MAP. This could be expected, because the knowledge of the image classes provides no direct information about the lesions (since the lesions only affected a few pixels from a single class). It seems also in line with [1], [2], where similar noise performance was found for post-smoothed MLEM and MAP for the case of matched spatial resolution.

The loss of information present in neighboring pixels is effectively reduced or eliminated with the prewhitening measure Q_2. Apparently, the information present in the unconstrained MLEM image is very similar to that present in the original sinogram data, and it can be recovered if the noise covariance is taken into account. Unfortunately, the method involves the application of a shift variant filter, making the implementation more complicated than that of MAP.

It has been found that both humans and nonprewhitening observers perform better with moderate smoothing [11], [15], [16], [17]. Our experiment illustrates that the low pass filter acts as an approximation of the ideal prewhitening filter. Figure 5 shows that when the approximate prewhitening filter becomes wider, the optimal Gaussian kernel is wider as well. The approximate prewhitening filter can be used to implement numerical observers with (partial) prewhitening, such as the channelized Hoteling observer [15], as shown (for both MLEM and MAP) by Bonetto et al [14].

Although good agreement between human observers and nonprewhitening observers has been reported [7], [18], recent studies indicate that human performance is better predicted by the channelized Hoteling observer [15], [16], [19], which has limited prewhitening capabilities. Consequently, results obtained with the nonprewhitening observer cannot be extrapolated to humans without additional experiments. However, in the case of smoothing within anatomical boundaries, high frequency noise is strongly suppressed. As it is unlikely that humans detect (very) low frequency noise correlations, it is expected that human performance will show similar trends as the nonprewhitening observer for this application.

References

[1] J Nuyts, JA Fessler, “A penalized-likelihood image reconstruction method for emission tomography, compared to post-smoothed maximum-likelihood with matched spatial resolution.” *IEEE Trans Med Imaging,* vol 22, pp 1042-52, 2003.

[2] JW Stayman, JA Fessler, “Compensation for nonuniform resolution using penalized-likelihood reconstruction in space-variant imaging systems,” *IEEE Trans Med Imaging,* to appear.

[3] K Baete, J Nuyts, W Van Paesschen et al. ”Evaluation of an antomical based MAP reconstruction algorithm for PET in epilepsy.” Accepted at the IEEE NSS and MIC, october 2003.

[4] LS Shepp, Y Vardi, “Maximum likelihood reconstruction for emission tomography,” *IEEE Trans Med Imaging,* vol MI-1, pp. 113-122, 1982.

[5] MH Hudson, RS Larkin, “Accelerated image reconstruction using ordered subsets of projection data,” *IEEE Trans Med Imaging* vol 13, pp. 601-609, 1994.

[6] J Nuyts, D Bequé, P Dupont et al. ”A concave prior penalizing relative differences for maximum-a-posteriori reconstruction in emission tomography.” *IEEE Trans Nucl Sci,* vol 49, pp 56-60, 2002.

[7] HH Barrett, J Yao, JP Rolland et al. “Model observers for assessment of image quality”. *Proc Natl Acad Sci USA* vol 90, pp 9758-9765, 1993.

[8] HH Barrett, JL Denny, RF Wagner et al. “Objective assessment of image quality. II. Fisher information, Fourier crosstalk, and figures of merit for task performance”. *J Opt Soc Am A,* vol 12, pp. 834-852, 1995.

[9] KV Mardia, JT Kent, JM Bibby. “Multivariate analysis”. Academic, San Diego, Calif., 1979.

[10] HH Barrett, DW Wilson, BMW Tsui. “Noise properties of the EM algorithm: I. Theory”. *Phys Med Biol,* vol 39, pp. 833-846, 1994.

[11] J Qi, RH Huesman. “Theoretical study of lesion detectability of MAP reconstruction using computer observers.” *IEEE Trans Med Imaging,* vol 20, pp 815-822, 2001.

[12] J Qi, RM Leahy. “Resolution and noise properties of MAP reconstruction for fully 3-D PET.” *IEEE Trans Med Imaging,* vol 19, pp. 493-506, 2000.

[13] JA Fessler. “Mean and variance of implicitly defined biased estimators (such as penalized maximum likelihood): applications to tomography”. *IEEE Trans Image Processing,* vol 5, pp. 493-506, 1996

[14] P Bonetto, J Qi, RM Leahy. “Covariance approximation for fast and accurate computation of channelized Hotelling observer statistics.” *IEEE Trans Nucl Sci* vol 47, pp. 1567-1572.

[15] HC Gifford, MA King, MV Narayanan et al. MS SMyczynski, RG Wells. “Effect of block-iterative acceleration on Ga-67 tumor detection in thoracic SPECT”. *IEEE Trans Nucl Sci,* vol 49, pp. 50-55, 2002.

[16] CK Abbey, HH Barrett. “Human and model observer performance in ramp-spectrum noise: effets of regularization and object variability”. *J Opt Soc Am A,* vol 18, pp. 473-488, 2001.

[17] K Baete, J Nuyts, W Van Paesschen et al. Dupont. “Anatomical based FDG-PET reconstruction for the detection of hypometabolic regions in epilepsy.” *Proceedings of the IEEE NSS and MIC,* November 10-16, 2002, Norfolk, VA, USA.

[18] DJ de Vries, MA King, EJ Soares et al. “Effects of scatter subtraction on detection and quantitation in hepatic SPECT studies”. *J Nucl Med,* vol 40, pp. 10011-1023, 1999.

[19] HC Gifford, MA King, DJ de Vries et al. “Channelized Hotelling and human observer correlation for lesion detection in hepatic SPECT imaging.”. *J Nucl Med* vol 41, pp. 514-521, 2000.